Assessing Composite Structure in Metal-Organic Framework-Polymer Mixed-Matrix Membranes

Avery E. Baumann[1*], Peter A. Beaucage[1,2], Richard Vallery[3], David Gidley[4], Ryan C. Nieuwendaal[1], Chad R. Snyder[1], Jan Ilavsky[5], Fu Chen[6], Christopher M. Stafford[1], Christopher L. Soles[1]

[1]Materials Science and Engineering Division, National Institute of Standards and Technology, Gaithersburg, MD 20899, USA

[2] Center for Neutron Research, National Institute of Standards and Technology, Gaithersburg, MD 20899, USA.

[3]Department of Physics, Grand Valley State University, Allendale MI 49401, USA

[4] Department of Physics, University of Michigan, Ann Arbor, MI 48109, USA

[5]X-Ray Science Division, Advanced Photon Source, Argonne National Laboratory, Lemont, IL 60439, USA

[6] Department of Chemistry and Biochemistry, University of Maryland, College Park, MD 20742, USA

* Corresponding author email avery.baumann@nist.gov

Abstract

Metal-organic frameworks (MOFs) are renowned for their tunable structure, porosity, and internal chemistry with demonstrated applications in molecular separations, storage, and conversion. While they are widely usable, the powdery characteristics of MOF materials can be limiting for large-scale processing and implementation in devices. Incorporating MOF particles into polymer supports affords engineering solutions to overcome these issues, yet the nature of the resulting composites is difficult to assess. In this work, we present spectroscopic and calorimetric methods that we believe help establish a holistic physico-chemical picture of the composite structure using a series of Zr MOFs with different pore sizes as a testbed. Power law decays are observed in X-ray scattering profiles in low q-space ranging between 2.4 to 3.3, which we interpret as changes in scattering contrast due to polymer infiltrating MOF particles. This interpretation is supported by solid-state nuclear magnetic resonance spectroscopy and differential scanning calorimetry measurements that identify populations of MOF-associated polymer. Additionally, positron annihilation lifetime spectroscopy measurements collected on a series of composites with different MOF-

polymer ratios show multiple decay constants each correlated to a different free volume element. In combination with the spectroscopic, calorimetric and scattering results, we utilize the trends in decay constants as a function of polymer mass fraction to hypothesize a polymer infiltration mechanism whereby large pores are preferentially filled, followed by small pores and, later still, interstitial spaces between particles. Even with vigorous investigation of polymer, MOF, and interface characteristics, the complex and heterogeneous nature of the composites makes absolute structural assertions difficult. We envision the approaches demonstrated here will be a useful foundation to assess and ultimately guide the design of future MOF-polymer composites.

Introduction

Metal-organic framework (MOF)-polymer mixed-matrix membranes and similar non-membrane composites are growing in importance for separations, energy storage, and chemical warfare agent degradation.[1–6] The ability to encase a MOF in a polymer matrix enables applications where a free-flowing powder is not an appropriate form factor such as in industrial filtration, face mask, or electronic sensing devices. Beyond membrane applications, solution processing of MOF-polymer composites is desirable for coating fabrications in membrane contactors or heat exchange systems.[7–9] Numerous studies have identified MOF-polymer combinations for tailored applications, but only a handful have characterized the detailed nature of the MOF-polymer interactions in the composite.[10–17] As these composites continue to evolve,

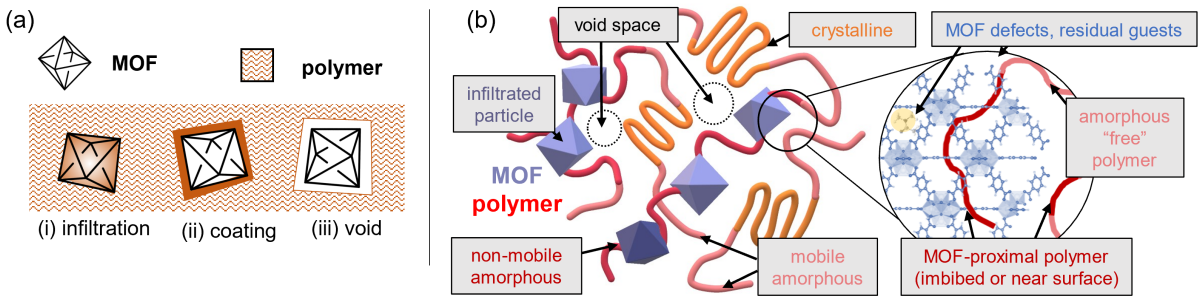

Scheme 1. (a) Combination of MOF and polymer in solution creates a slurry that can cast to form mixed-matrix membranes. General MOF-polymer interaction can be described by (i) pore infiltration, (ii) surface coating, and (iii) void inclusion models. (b) Structural attributes possible within MOF-polymer composites that add complexity to characterization.

rapid and informative characterization techniques are needed to understand and predict structure-property relationships as well as guide the design of the MOF-polymer combinations for specific applications. This paper demonstrates how some techniques established to study the properties of polymers and porous materials are also well-suited to provide quantitative descriptors of MOF-polymer composites beyond typical qualitative characterization. Further, we show how these measurements conducted on series of isoreticular Zr MOFs dispersed/mixed with polymer at different concentrations provide critical insight into mechanisms of pore filling.

From a simple viewpoint, MOF-polymer composites can exist in several forms illustrated in **Scheme 1a** where the (i) polymer infiltrates the porous MOF structure, (ii) polymer completely coats the MOF crystallite, and (iii) polymer incompletely covers the MOF crystallites (creating voids in the matrix), each with varying consequences to the permeability and selectivity of the membrane.[1,4] In actuality, there are much more complex structural aspects to consider including polymer crystallinity, mobile vs. non-mobile amorphous polymer fractions, and various MOF-polymer interactions that can manifest within the different structural classes of composites (**Scheme 1b**). Differentiating these structures represents a challenge for the materials community as characterization methods that can assess degrees of infiltration or void inclusion across a diverse MOF-polymer compositional spaces have not yet been suitably established.

Schmidt-Rohr, Cohen and coworkers presented that solid-state nuclear magnetic resonance (NMR) spectroscopy can be a valuable tool to differentiate between infiltration regimes (shown in **Scheme 1a**) by quantifying interactions between the organic linkers of the MOF and polymer chains in polyethylene oxide

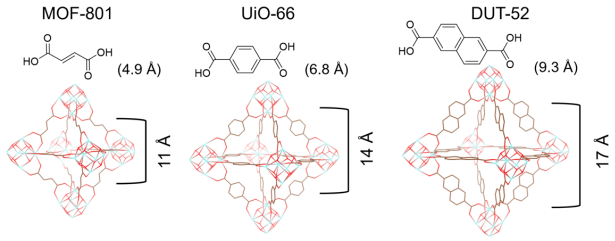

Scheme 2. Linker and octahedral pore geometries for the series of 12-connected Zr MOFs utilized in this study (MOF-801, UiO-66, DUT-52). Listed dimensions measured from crystallographic data from respective publications for each MOF.[18–20]

(PEO) and polyvinylidene fluoride membranes containing one MOF, UiO-66.[10] We expand upon this seminal work by conducting similar NMR analyses on a series of MOF/PEO composite membranes, while evincing that a deeper understanding of such systems can be obtained by enlisting additional characterization techniques including calorimetry, X-ray scattering, and positron annihilation lifetime spectroscopy. To establish this toolset, we systematically chose a series of MOFs (**Scheme 2**) to expressly explore the effects of the cage size on the infiltration of PEO into the MOF. It has been shown previously that PEO can infiltrate into the internal pores of UiO-66[10], but it is unclear to what extent infiltration will occur for analogous MOFs with larger or smaller pores. The numerous structural attributes ascribed to the individual MOF or polymer components, as well as those arising because of their mixing, imparts the underlying complexity of these composites and validates the need to investigate structures using multiple approaches.

Material Preparation & Validation

For this investigation, we examine a series of composites prepared with canonical 12-connected Zr MOFs of generic formula $Zr_6(\mu_3\text{-}O)_4(\mu_3\text{-}OH)_4(linker)_6$, where the linker identity varies to give specific MOFs including MOF-801, UiO-66, and DUT-52. The naming convention of some MOFs indicates their institution of origin, where "UiO" and "DUT" represent University of Oslo and Dresden University of Technology, respectively. These MOFs each have the same topology but vary in pore/linker sizes, as drawn in **Scheme 2**, and were selected to minimize differences in the internal pore chemistry and crystal habits. The MOFs are mixed with a high molar mass PEO (viscosity average molecular mass ≈ 900 kg mol^{-1}) capable of forming free-standing composite membranes.

The different MOF powders were synthesized following a previously reported procedure as described in the Supporting Information.[10] Although the MOFs selected for this study have different reported synthetic conditions in their respective publications containing crystallographic information[18–20], the same synthetic methods (metal/linker ratio, solvent media, temperature, reaction time) were employed

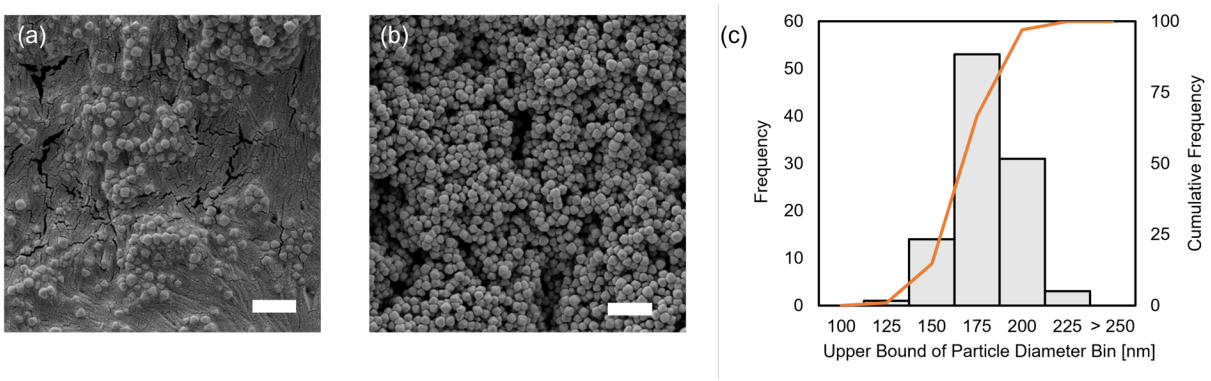

Figure 1. SEM images of sputter coated (a) 30/70 and (b) 70/30 composite UiO-66/PEO samples. The scale bar represents 1 μm in each panel. (c) The distribution of measured particle diameters for UiO-66 used in this study.

for each material synthesis in an attempt to minimize issues arising from defect incorporation, drastic differences in particle sizes/shapes, or similar structural variations identified in the field.[21–25]

The crystal structures of the synthesized MOFs were confirmed using powder X-ray diffraction (XRD, **Figure S1**) and compositionally characterized by thermogravimetric analysis (TGA, **Figure S2**).[18–21] Each MOF sample has a similar quantity of missing linkers per formula unit as assessed by TGA (0.81 to 1.02) and NMR analysis (0.95 to 1.27) as described in **Table S1**.[21,26,27] These values indicate roughly one sixth of the linkers are missing, which is not unusual for the UiO-66 family of MOFs.[21] The MOF-801 sample is slightly less homogenous than the UiO-66 and DUT-52 samples as evidenced by both the relative decrease in intensity and broadness of the XRD peaks and multiple linker-attributed mass loss events in the TGA results (**Figures S1-S2**). This is to be expected based on the original report, which included several contributing structures resolved from diffraction data and a similar TGA result.[18]

With verification of the MOF structures, the PEO based composites were prepared using calculated mass ratios of a 3.5 % aqueous PEO solution and a suspension of 3.5 % MOF in acetone to yield samples of 30/70, 50/50, and 70/30 MOF/PEO by mass fraction. The mixture was sonicated, concentrated under reduced pressure, and the viscous slurry was blade cast onto aluminum foil at a set height of 1 mm as described in a previous report.[10] The cast mixtures were dried at 70 °C in a vacuum oven for 3 h and peeled away from the foil support for further testing. Complete details of composite preparation can be found in the Supporting Information along with photographs of resulting free-standing membranes (**Figure S3**).

Scanning electron micrographs (SEM) of the 30/70 and 70/30 UiO-66/PEO samples in **Figure 1** show the noodle-like domains of PEO (visible in the 30/70 sample) and small MOF particles distributed throughout the composite. SEM images of the other MOF/PEO composites are visually similar to the UiO-66 composite samples (**Figure S4**), although the particle size of the MOFs is less homogeneous in those cases. The particle diameter distributions measured for the as-prepared MOF powders are presented in **Figure 1c** for UiO-66 and **Figure S5** for all three MOF powders. The average size of the MOF particles is roughly 200 nm. UiO-66 has a ± 30 nm narrower distribution of particle diameters than MOF-801 and DUT-52.

The MOF/PEO composition of the prepared membranes was measured gravimetrically for each composite. TGA curves are compared at 30/70 and 70/30 MOF/PEO across the MOF series in **Figure 2a** (and at various loadings within the same MOF series in **Figure S6**), where the mass loss attributed to PEO matches the initial formulation recipe target within 3 % variance by mass. The crystal forms of the MOFs within the composite membranes were verified by XRD (**Figure S7**), where the characteristic diffraction peaks corresponding to the MOF structure are identified in each sample and crystalline PEO features begin to appear in composites with higher polymer loadings.

Characterization of Composite Structures

Differential Scanning Calorimetry

Differential scanning calorimetry (DSC) experiments reveal information about both the crystalline and amorphous fractions of PEO in the composite. Using a combination of DSC and modulated DSC thermograms, we identify the crystal fractions, the crystal sizes, and the populations of polymer chains in the rigid and mobile amorphous phases. The absolute polymer crystallinity is determined by integration of the PEO melt event around 60 °C in the heating segment of the DSC scans (**Figure 2b**, all compositions shown in **Figure S8**). The PEO melting transition is obvious at low MOF loadings but is significantly diminished at high MOF loadings as the polymer chains associate with filler particles or infiltrate within the porous MOF structure, a common observation for these types of composites.[15,28–30] We report the

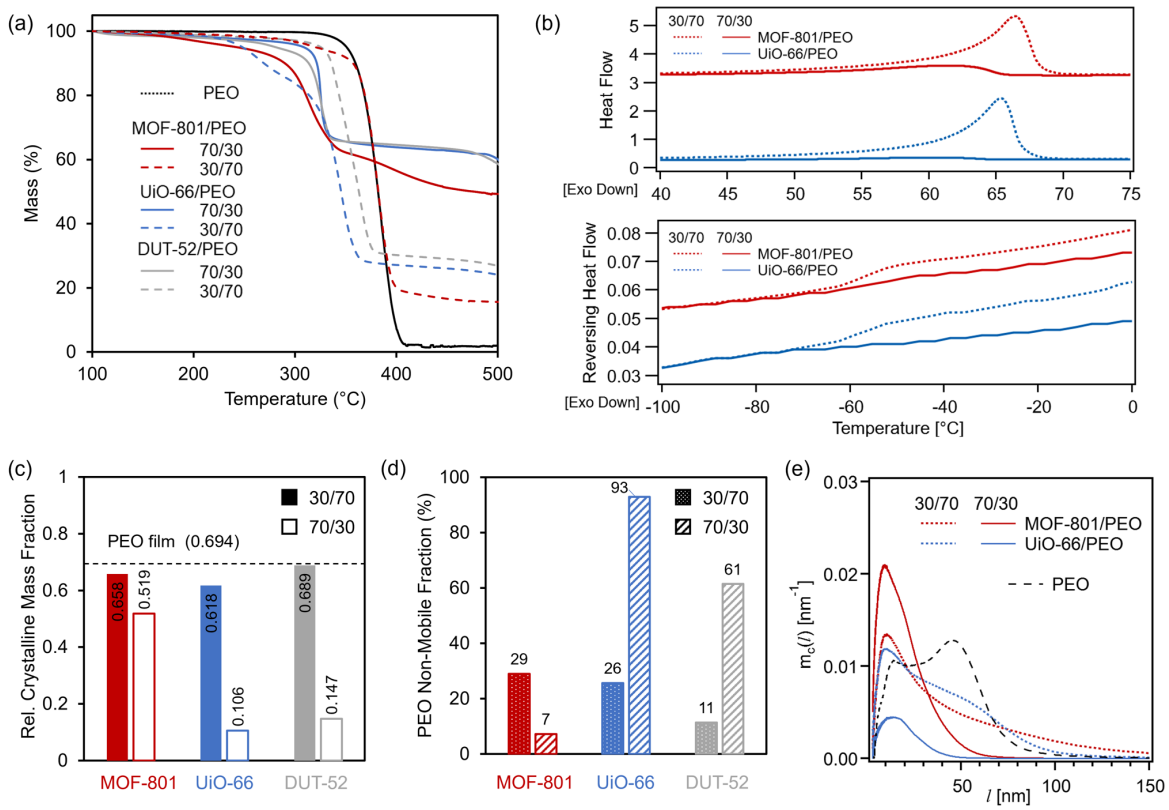

Figure 2. (a) TGA profiles for 30/70 (dashed lines) and 70/30 (solid lines) MOF/PEO samples compared to PEO (dotted line). PEO mass loss occurs below 450 °C. The measured PEO mass % agrees with the formulated compositions within 3 %. (b) Individual DSC scans for PEO melting (top) and glass transition (bottom, via temperature modulated DSC) events for several MOF/PEO composites. (c) Compiled DSC peak integration of the melting event yields the observed crystalline mass fraction of PEO relative to the total mass of PEO in the composite (a value of 1 would indicate a 100 % crystalline PEO sample). The dashed line represents the measured fraction of crystalline PEO in the film cast in the same manner as the MOF/PEO samples. Uncertainty is determined to be less than 6 % (1 standard deviation) of the integration from 3 repeated heating/cooling cycles. (d) Non-mobile fraction of PEO determined from temperature modulated DSC experiments. (e) Mass normalized PEO crystallite size distribution determined from the melting event in DSC experiments.

measured mass fraction of crystalline PEO relative to the total amount of PEO in the sample for each different film in **Figure 2c**. The quantities are normalized so that a value of 1 represents the enthalpy of fusion for 100 % crystalline PEO[31], allowing us to compare different film compositions directly. In the 70/30 MOF/PEO composites, we measure a larger fraction of crystalline PEO in MOF-801 (0.519) than in the UiO-66 and DUT-52 containing samples (0.106 and 0.147, respectively). From this result, we hypothesize the smaller pores in MOF-801 inhibit PEO infiltration causing more polymer to remain outside the MOF structure where crystallization can occur. In comparison, the UiO-66/PEO and DUT-52/PEO

composite membranes contain roughly one fourth of the amount of crystalline polymer relative to MOF-801/PEO despite the same 70/30 MOF/PEO composition.

Quantifiable differences in polymers chains entering the pores of the MOF samples are further supported by an analysis of the glass transition of PEO using temperature modulated DSC scans in **Figure 2b**. PEO's rigid amorphous fraction (RAF) devitrifies at approximately the glass transition temperature (≈ -50 °C)[32], so any reduction in the change in heat capacity at the glass transition temperature that is not attributable to the crystalline fraction can be associated with some other immobilized amorphous fraction.[32] A mass balance analysis can thus quantify amorphous material that has been restricted by the MOF (non-mobile fraction, NMF) separate from the mobile amorphous fraction (MAF) as indicated in eq. 1. Including the RAF in the MAF, yields the following relationship for the mass fraction of the non-mobile fraction (m_{NMF}):

$$m_{NMF} = 1 - m_c - m_{MAF} = 1 - m_c - \frac{\Delta C_{p,sc}}{\Delta C_{p,am}} \qquad \text{(eq. 1)}$$

where m_c is the crystalline mass fraction, m_{MAF} is the mass fraction of the mobile amorphous fraction, and $\Delta C_{p,am}$ and $\Delta C_{p,sc}$ are the step in heat capacity of a 100 % amorphous sample (determined from measurements on the neat PEO sample and its m_c) and semicrystalline sample, respectively. In **Figure 2d**, we plot the fraction of the total amorphous material that is non-mobile, i.e., $m_{NMF}/(m_{MAF} + m_{NMF})$, for the 30/70 and 70/30 MOF/PEO samples. The non-mobile fraction of PEO in the 70/30 composite only is ≈ 7 % for the MOF-801 sample compared to ≈ 61 % and ≈ 93 %, for the DUT-52 and UiO-66 containing samples, respectively. This value represents a percentage of the amorphous material that has been restricted by the MOF, either through incorporation into the MOF structure or via surface interactions. While we would expect DUT-52 to imbibe more PEO than UiO-66 owing to the longer linker and therefore greater pore size, these results hint that there may be other factors controlling polymer infiltration into the MOF structures such as variation in surface termination or other particle characteristics.

PEO crystal size can be measured from the DSC data as well, which can be important in both the mechanical and transport properties of the MOF/PEO membrane. In particular, we calculate the PEO crystallite thickness perpendicular to the basal plane (l) by normalized mass (m_c) of PEO in a manner similar to Crist and Mirabella[33] using equations S1 through S3 in the Supporting Information.[31,34–40] Henceforth, for simplicity we will refer to l as the "crystal size", but it should be recognized this is first and foremost a measure of crystal size in the direction of the polymer backbone.[38] The resulting crystal size distributions for MOF-801/PEO and UiO-66/PEO composites are plotted in **Figure 2e**. Size distributions of PEO in DUT-52/PEO composites, which are similar to those of UiO-66/PEO, are represented in **Figure S8** for clarity. We find the appearance of larger crystallites as the mass fraction of PEO in the composite increases, such as in the 30/70 MOF/PEO samples where characteristic crystal thickness spans roughly 150 nm. In each of the 30/70 MOF/PEO composites, the PEO crystallites are classified into roughly bimodal populations with thicknesses around 10 nm and 50 nm that match the analogously prepared PEO film. When the MOF mass fraction is increased, the larger mode is significantly diminished in all composites.

The MOF-801/PEO composite contains a much larger mass fraction of crystalline PEO with a wider size distribution (< 65 nm) than either the UiO-66 or DUT-52 composites (< 50 nm) at the same 70/30 MOF/PEO composition. Since the MOF particles are roughly the same size and vary only slightly in crystallographic density, we can rule out that this difference in PEO crystallinity arises from simple particle packing effects. The larger mass fraction of bigger PEO crystallites in MOF-801 composites indicates a more PEO-rich domain outside MOF particles where crystallization can occur, supporting our hypothesis that infiltration is suppressed in MOF-801. This observation is also consistent with the smaller amount of MOF-associated PEO in MOF-801 composites relative to UiO-66 and DUT-52 composites, which will be described further in the next section.

NMR Spectroscopy

To characterize the MOF and amorphous polymer domains, we next provide a detailed analysis of MOF-polymer interactions by utilizing previously demonstrated ^{1}H-^{13}C cross-polarization magic angle

spinning (CPMAS) NMR spectroscopy methods.[10,41] The ^{13}C CPMAS spectra for the three 70/30 MOFs with PEO are given in **Figure 3**; those without PEO are given in **Figure S9**. The largest peaks are those associated with the MOF linkers, which are sp^2 carbons in the range of 120 ppm to 175 ppm (where a chemical shift of 1 ppm corresponds to 125 Hz), and smaller resonances associated with physisorbed molecules from the MOF synthesis (DMF and dimethylamine, labeled with +, or acetate or formate labelled with #). We observe significant fractions of DMF in all samples despite repeated solvent-exchange steps during material preparation. Indeed, we calculate DMF/linker molar ratios of 0.57, 0.24, and 0.38 for the MOF-801, UiO-66, and DUT samples, respectively (**Table S2**). These ratios decrease to 0.42, 0.05, and 0.03 in samples with PEO, which indicates the DMF is largely removed by PEO infiltration in UiO-66 and DUT-52 samples. It is unlikely that DMF in MOF-801 prevents PEO incorporation, but rather that inaccessibility to internal pores limits PEO exchange with DMF. Acetate- and formate-based defect sites (peaks labeled # in the spectra) are observed in smaller populations than the linker. CPMAS quantification estimates agree with the calculated defect values of one missing linker out of six per formula unit (where it is assumed two acetate or formate molecules replace each linker at node coordination sites) calculated from the TGA and digested MOF solution NMR measurements (**Table S1**).

Upon incorporation of PEO, we observe clear changes in the ^{13}C chemical shift positions and linewidths of the linker resonances. These shifts in chemical shifts (**Table 1**) are due to changes in the local environment of the linker due to interaction with guest molecules, and the broadening is due to an increased polydispersity of molecular bonding environments in the composite. In the MOF/PEO samples, we also observe the ethylene oxide resonance in the CPMAS spectrum at 70.0 ppm. We observe two overlapping PEO peaks (rightmost panels in **Figure 3**): a narrow peak which we ascribe to free (non-crystalline) PEO, and a broad peak which we ascribe to (non-crystalline) PEO chains that are in spin diffusion contact with the MOF linkers, referred to from here on as “proximal PEO”.[42] We note that while there are likely PEO chains on the surfaces of the MOF crystals that are also in spin diffusion contact, at these observed MOF particle sizes (> 160 nm) the volume fraction of this population is quite low (< 5 %). Despite PEO crystals

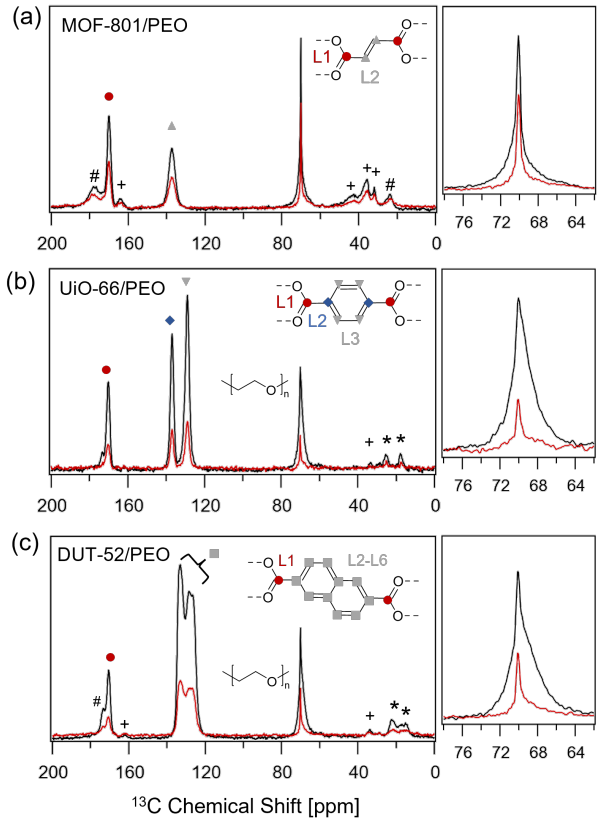

Figure 3. ^{13}C CPMAS NMR spectra of 70/30 (a) MOF-801/PEO, (b) UiO-66/PEO, and (c) DUT-52/PEO composites. The linker resonances are labeled in each figure with filled shapes. Spinning sidebands (*), DMF and carboxylate derivates imparted from the MOF synthesis are denoted with (+) and (#) symbols. Spectra acquired without (black) and with (red) an applied 5 ms spin lock pulse demonstrate the decay in signal intensity used to calculate $T_{1\rho}$ values. The rightmost panels are enlarged to show the overlapping PEO peaks.

observed from DSC in the 70/30 samples, no crystalline PEO resonance is observed in the CPMAS spectra due to the short $T_{1\rho}$ (0.1 ms) relative to the contact time (2 ms).[42] We deconvolve the overlapping PEO resonances (emphasized in the rightmost panels in **Figure 3**) to determine the MOF-proximal molar fraction of polymer which follows the trend MOF-801 << DUT-52 < UiO-66, consistent with our DSC analysis.

In order to investigate local proximities of PEO (or other minor guest molecules) and MOF species, we adopt the method demonstrated by Schmidt-Rohr, Cohen and coworkers which utilizes $T_{1\rho}$-relaxation with ^{13}C detection.[10] In this experiment, a spin-lock pulse of duration τ_s causes the ^{1}H nuclear spin polarization to decay with the time constant $T_{1\rho}$. Fast relaxing spins, such as those involved in segmental dynamics on the 10 μs timescale in PEO, will spin exchange with ^{1}H atoms in more rigid environments

(such as in the MOF) relating a timescale change of relaxation that is a measurement of proton-proton proximities between the components. We insert a spin-lock pulse at the beginning of cross-polarization sequence so ^{13}C polarization decays by virtue of ^{1}H-to-^{13}C cross polarization. The resultant spectra with τ_s = 5 ms are given in **Figure 3** (red traces). To a first approximation, adjacent ^{1}H spins exhibit a common $T_{1\rho}$ due to spin diffusion, and remote ^{13}C spins (at distances longer than the ^{1}H spin diffusion radius, r_{SD}), will exhibit different $T_{1\rho}$ times. The $T_{1\rho}$ values are 1 ms to 10 ms, so assuming the spin diffusion coefficient is between 0.4 $nm^2\ ms^{-1}$ and 0.8 $nm^2\ ms^{-1}$, Fick's law predicts r_{SD} to be 1 nm to 5 nm, which encompasses the MOF unit cell.[43] The NMR peak intensity with the spin lock pulse (I) relative to that without spin lock pulse (I_0) was measured for a pulse length (τ_s) of 5 ms, and the $T_{1\rho}$ was calculated via eq.2:

$$I = I_0 \exp(\frac{-\tau_s}{T_{1\rho}}) \qquad \text{(eq. 2)}$$

The extracted $T_{1\rho}$ values for the MOF and PEO peaks in the ^{13}C spectra are given in **Table 1**. The linker peaks of all the neat MOF samples exhibit long $T_{1\rho}$ values (12.5 ms to 21 ms) for all samples. In the neat MOFs, the DMF peaks (**Table S2**) exhibit similar values to the linkers in MOF-801, suggesting the DMF is well dispersed within the MOF-801 particles. However, distinctly shorter $T_{1\rho}$ times are measured for the DMF in neat UiO-66 and DUT-52, indicating that DMF is preferentially located within MOF particles near walls/surfaces rather than in pore void space. This would be consistent with coordination leading to residual DMF persisting even after solvent exchange steps performed during sample preparation.

Upon incorporation of PEO, drastically smaller $T_{1\rho}$ values are observed for the linker ^{13}C peaks as compared to the neat samples, indicating the PEO protons are mixed with the MOF protons on length scales of the spin diffusion radius (< 5 nm) in each of the samples. Upon inspection of the PEO resonances (70.0 ppm), we find that short $T_{1\rho}$ values (2.5 ms to 4.9 ms) are exhibited for the broad peak associated with proximal PEO, and long $T_{1\rho}$ times (15 ms to 20 ms) are exhibited for the narrow peak associated with free PEO chains consistent with previous studies.[10] In all three samples, the proximal PEO $T_{1\rho}$ is shorter than the MOF linker $T_{1\rho}$ time, which unambiguously shows that (1) PEO does not completely fill the MOF particles, and (2) PEO chains do not pack uniformly throughout the MOF particles. Rather, there are distinct

Table 1. ^{13}C NMR chemical shift positions, assignments, relative intensities, and ^{1}H-associated $T_{1\rho}$ values of the three MOF samples both with and without PEO. The proximal and free fraction of the total PEO intensity is determined from the relative intensity of the broad and narrow peak, respectively.

	MOF			70/30 MOF/PEO		
Peak Assignment	**Peak Position (ppm)**	**Relative Intensity**	**$T_{1\rho}$ (ms)**	**Peak Position (ppm)**	**Relative Intensity**	**$T_{1\rho}$ (ms)**
MOF-801						
Linker COO (L1)	169.5	0.26	19.5 ± 1.0	169.9	0.20	7.2 ± 0.4
Linker HC=CH (L2)	137.0	0.26	19.5 ± 1.0	137.2	0.21	7.2 ± 0.4
Non-crystalline PEO (total)				70.0	0.21	-
Proximal Fraction					*0.8*	4.9 ± 0.5
Free Fraction					*0.2*	20 ± 5
UiO-66						
Linker COO (L1)	168.9	0.17	16.0 ± 1.5	170.3	0.16	3.8 ± 0.5
Linker Arom. C-C (L2)	136.9	0.25	15.0 ± 0.7	137.1	0.24	4.0 ± 0.5
Linker Arom. C-H (L3)	127.8	0.49	13.0 ± 1.0	129.0	0.38	3.8 ± 0.5
Non-crystalline PEO (total)				70.0	0.19	-
Proximal Fraction					*0.93*	2.5 ± 0.5
Free Fraction					*0.07*	17 ± 4
DUT-52						
Linker COO (L1)	169.7	0.12	12.5 ± 0.8	170.6	0.11	3.8 ± 0.5
Linker Arom. C (L2 – L6)	133.0, 126.3	0.78	13.5 ± 0.5	133.1, 127.7	0.75	4.2 ± 0.4
Non-crystalline PEO (total)				70.0	0.127	-
Proximal Fraction					*0.9*	2.6 ± 0.3
Free Fraction					*0.1*	15 ± 2

regions of PEO-filled MOF and unfilled (or underfilled) MOF. If we assume that the observed linker $T_{1\rho}$ time is simply a weighted average of neat MOF domains and PEO-filled domains, then the fraction of PEO-filled MOF domains follows the trend MOF-801 << DUT-52 < UiO-66, a trend that agrees with our temperature modulated DSC analysis.

More sophisticated modeling of the change in MOF linker $T_{1\rho}$ values is not straightforward since the relative intensities of the linker peaks display inconsistent changes in samples with and without PEO, despite being on the same molecule (**Table 1**). For instance, if we compare the carbonyl carbon of the linker

(labeled "L1" and with red circle in **Figure 3**), the relative $T_{1\rho}$ values for MOF-801, UiO-66, and DUT-52 are 2.7, 4.2, and 3.3 times faster upon introduction of PEO whereas relative $T_{1\rho}$ values for "L2" are 2.7, 3.8, and 3.2 times faster, respectively. We also caution the readers that these values should be used relative to one another for comparisons since $T_{1\rho}$ uncertainties as high as 25 % and 13 % are observed for the PEO and MOF linker peaks, respectively (listed in **Table 1**). These uncertainties, which are due primarily to the signal/noise ratios and uncertainties in ^{1}H-^{13}C cross-polarization kinetics at high MAS, prevent us from commenting further on these $T_{1\rho}$ differences, which could presumably be due to the degree and uniformity of polymer loading into the MOF particles. Future studies using more quantitative CPMAS methods, such as lower MAS at lower field[43,44] or multi-CP sequences[45], could help us understand the uniformity of polymer packing and dynamics in the MOF particles.

X-ray Scattering

Small angle X-ray scattering (SAXS) is widely employed in the polymer and polymer-composite communities to examine domain sizes, organizational morphologies, and dynamic processes of chain folding and rearrangement.[46] Conventional in-house SAXS is typically suited for length scales from 1 nm to 100 nm and can be obtained in various environmental conditions and with small sample sizes. A more expansive range of length scales can be achieved at many synchrotron sources, such as the Advanced Photon Source (APS) at Argonne National Laboratory, enabling collection of ultra-small angle (USAXS) and wide-angle (WAXS), along with conventional SAXS, scattering data spanning length scales of greater than five orders of magnitude (μm to Å resolution) in minutes.[47–49] Depending on the system, a vast amount of qualitative and quantitative information can be extracted from scattering profiles that is pertinent to mixed-matrix membranes including aggregation, particle/domain sizes, size dispersity, and interface characteristics that are useful in characterizing composite samples.

Data collected at APS were reduced and analyzed using the *Indra/Irena* software packages, yielding the X-ray scattering profiles for PEO and MOF/PEO composites shown in **Figure 4a-b**.[50,51] The

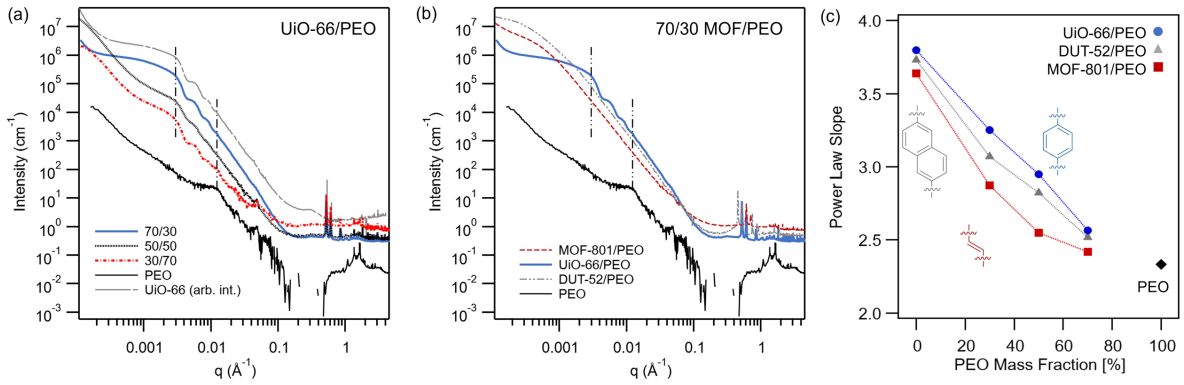

Figure 4. X-ray scattering profiles for (a) the UiO-66/PEO composite series prepared at different MOF/polymer loadings, and (b) all the 70/30 MOF/PEO samples prepared with different MOF identities. The scattering profile of a cast PEO film is appended to both (a-b). The power law relationship as measured by the slope between the dotted vertical lines in (a-b) for the various composites are compiled in panel (c) and connected by lines to guide the eye within a MOF/PEO series. The power law slope for PEO was obtained between 0.02 Å^{-1} and 0.1 Å^{-1} on the log-log plot.

scattering profile for the neat polymer film (black traces, **Figure 4a-b**) exhibits a Gunier peak around 0.012 Å^{-1}, and relatively low scattering at smaller q. The larger size of the PEO crystallites determined from our DSC measurement (roughly 50 nm, **Figure 2e**) is consistent with this dimension in reciprocal space (using the conversion to real-space dimensions $d = 2\pi/q$). Since the scattering profiles containing MOF particles show orders of magnitude stronger scattering than PEO at $q < 0.012$ Å, we can attribute scattering intensity in this range to MOF features in the composite samples. We find UiO-66/PEO composites feature nearly monodisperse MOF particles with size of 190 nm by fitting the periodic scattering features using a spherical particle model.[52] The scattering profiles of both MOF-801/PEO and DUT-52/PEO samples do not display these periodic features due to increased dispersity in particle size and could not be fit with the same level of confidence (**Figure 4b** and **Figure S10**). USAXS profiles of the neat MOFs show the same dispersity, indicating (1) the heterogeneity does not arise from addition of PEO and (2) MOF particle size is not changing with PEO infiltration (**Figure S11**). For the UiO-66 samples, the spherical particle size fit results are in good agreement with measured MOF particle sizes obtained using SEM (size histograms depicted in **Figure S5**), where UiO-66 particles are 168 nm ± 18 nm in diameter. The particle size in the 70/30 UiO-66/PEO composite (including sputtered ≈ 12 nm AuPd coating) was measured to be 185 nm ± 33 nm in diameter, further indicating the MOF particle size is not changing within statistical relevance.

Analysis of the Porod region, which describes the nature of scattering decay and manifests as a sloped downward line, is straightforward and perhaps the most informative for this system as it conveys surface and interface characteristics.[53] The Porod region for the MOF particles in this study is bounded between q = 0.012 Å^{-1} to q = 0.003 Å^{-1}, marked by dashed vertical lines in **Figures 4a-b**. As indicated in eq. 3, Porod's law states the relationship between scattering intensity ($I(q)$) varies as q^{-4} for smooth 3-D objects in a two-phase system with contrast ($\Delta\rho$) and surface to volume ratio (S/V) seen by the incident X-ray beam.[54]

$$I(q) = 2\pi\frac{S}{V}(\Delta\rho)^2 q^{-4} \qquad \text{(eq. 3)}$$

In more complex systems where the interface is less smooth or sharp, as is the case with coiled polymer chains or low-D objects, the power law dependence of $I(q)$ is related to the dimensionality of the object describing the system expressed by α in eq. 4. The slope of the linear portion of the curve yields the value α in a log-log plot. In the MOF/PEO composites, the power law slope continuously decreases with increasing PEO mass fraction (**Figure 4c**). We attribute this change in α to a change in the electron density within the MOF particles, where pore voids are infiltrated with PEO. If the particles were not infiltrated with polymer, we hypothesize that α would remain close to the value measured for MOF powders (≈ 3.7) regardless of PEO mass fraction.

$$I(q) \approx q^{-\alpha} \qquad \text{(eq. 4)}$$

Analysis of the power law slope in the low q-space (between the dashed vertical lines in **Figure 4a-b**, attributed to scattering from the MOF particles themselves) yields a range of α between 2.4 to 3.3 for MOF/PEO composites and ≈ 3.7 for MOF powders as plotted in **Figure 4c.** Uncertainty in these values is smaller than ± 0.1 determined by least-squares fitting method in the *Irena* software package and is further analyzed using a sequential step fitting algorithm (details and uncertainties provided in **Table S3**).[51] Across the different MOF/PEO series, we measure an increase in α at each of the respective PEO loadings following the order MOF-801 < DUT-52 < UiO-66. The difference among the MOF composites at the same

mass fraction of PEO tell us this is not a simple mixing-average, but that there is actual change in the scattering contrast at the MOF particle and matrix interface.

We are confident that the α parameter can be used to assess relative levels of polymer infiltration as the trends inferred from X-ray scattering are consistent with results obtained from other methods presented thus far (NMR, DSC). Furthermore, the universality of scattering contrast arising from electron density renders this approach applicable to composites that may not be amenable to investigation by CPMAS NMR (such as those featuring MOFs with paramagnetic ions or components that lack appropriate nuclei for cross-polarization) or DSC (such as those lacking thermal events that lie within the stability window of the MOF). We are unable to fit core-shell models or find a length scale of PEO in proximity to the MOF particles to further describe changes in particle surface/interface character using this X-ray scattering data, likely due to the heterogeneity of the interface. Considering these observations, we envision X-ray scattering analysis to be most useful in high-throughput screening experiments as opposed to more in-depth characterization by more time-intensive methods.

Positron Annihilation Lifetime Spectroscopy

Positron annihilation lifetime spectroscopy (PALS) is a powerful probe of internal porosity, with exceptional sensitivity to the sub-nm size pores that are germane to MOFs. In PALS, the positron lifetime(s) (τ_i) are measured as the time difference between creation of the positron, a radioactive decay product that is accompanied by a distinct gamma ray emission marking creation, and the subsequent annihilation event that occurs when the positron (Ps) annihilates with an electron in the sample. The annihilation event also emits a characteristic gamma with the time difference between these two gammas defining the Ps lifetime. The fraction of annihilation events corresponding to a given lifetime is reflected in relative intensity (I_i). Here, we are interested in the lifetimes and intensities of positrons that annihilate via long lived ortho-Ps (o-Ps, a triplet state where the positron and electron spins are parallel) since these events can be correlated with local regions of low electron density, consistent with intermolecular packing defects in the polymer[55] or internal pore spaces of the MOF[56]. o-Ps has a longer lifetime of 142 ns in vacuum that can

be strongly curtailed via interaction with matter, whereas para-Ps (a singlet state where the positron and electron spins are antiparallel) state has a much shorter lifetime (0.125 ns) that is largely unaffected by surrounding matter.[55] The o-Ps lifetimes are related to the free volume elements in which the o-Ps localizes before making contact with an opposite-spin electron from the denser regions of the sample and annihilating via the "pick-off" (singlet) mechanism. The connection between o-Ps lifetime and pores size is often quantified in terms of a spherical pore with radius *r* using the Tao-Eldrup model (eq. 5) with Δr = 0.166 nm.[57,58]

$$\tau = \frac{1}{2}\left[1 - \frac{r}{r+\Delta r} + \frac{1}{2\pi}\cdot \sin\left(\frac{2\pi\cdot r}{r+\Delta r}\right)\right]^{-1} \qquad \text{(eq. 5)}$$

In MOFs, PALS has been widely used to quantify the internal dimensions of the pores inside the MOF particles and can also provide insights into intergrain spacings by fitting the spectra with a range of different annihilation lifetimes.[14,56,59–61] The isolated UiO-66 powder used in this study yields several o-Ps lifetimes (corresponding to different pore radii) of τ_1 = 1.1 ns (1.8 Å), , τ_3 = 7.8 ns (6 Å), and τ_4 = 16.6 ns (8 Å) as listed in **Table S4** (τ_2 is attributed to the polymer in our assignments). While lifetimes on the order of τ_1 are observed in both MOFs and dense polymers, the longer lifetimes τ_3 and τ_4 are distinct characteristics of the internal pores in MOFs. Our results are slightly different than previously reported lifetimes for UiO-66[62,63] and correspond to some larger than expected pore sizes (from crystallographic dimensions) that are likely a result of delocalized o-Ps diffusing between domains through non-continuous pore walls and defective regions.[14] We also observe a very long, but low intensity o-Ps lifetime, τ_5, that is 130 ns to 140 ns. This is close to the in-vacuo lifetime of 142 ns for o-Ps and is strong evidence that after formation, a small fraction of the o-Ps can diffuse through the sample via interconnected pathways and escape into the vacuum chamber of the PALS instrument. This has previously been ascribed as intergrain hopping events in MOFs[61] and will be discussed in more detail later.

The annihilation lifetimes of the neat PEO film without MOFs are generally much shorter than the lifetimes in the MOFs. **Table S4** shows that pure PEO requires two lifetimes of τ_1 = 1.2 ns and τ_2 = 2.6 ns

to adequately fit the spectra. We suspect these two lifetimes represent the crystalline and amorphous domains in the PEO domains, but the details of such a separation are beyond the scope of this manuscript. Nevertheless, since the τ_1 and τ_2 of the neat PEO are convoluted with τ_1 from the neat MOF, we do not attempt to draw conclusions from their variations in the composite films.

We hypothesize that as PEO infiltrates into the internal pores of the MOFs, represented by τ_3 and τ_4, both the lifetimes and the intensities of those components will decrease relative to the unfilled MOF as their internal porosity is becoming occupied by guest polymer. A careful examination of data in **Table S4** reveals this trend to be true in a general sense. DUT-52 should have the largest pores based on its crystal structure, but we observe just a small addition of PEO quickly plugs up the pores. The largest pores (τ_4 signal) fill with a small addition of PEO; the smaller pores (τ_3 signal) fill up more slowly, but not until the highest PEO loadings. On the contrary, MOF-801 should have the smallest pores but exhibited longer average lifetimes than either of the UiO-66 or DUT-52 composites with similar gravimetric compositions despite MOF-801 featuring smaller crystallographic pore sizes. Internal electromagnetic differences, as well as defect presence inferred from TGA and PXRD characterization, could be contributing to longer lifetimes measured by PALS. The MOF-801 series shows a much weaker decrease in both τ_3 and τ_4 with PEO loading, indicating the filling mechanism differs. UiO-66 with the intermediate sized pores seems to fall between MOF-801 and DUT-52 in terms of the ability of infiltrating PEO to suppress the PALS signal.

As a general descriptor of PEO's ability to fill in the MOF pores, we average the MOF-centric PALS lifetimes τ_3 and τ_4 into a single average MOF lifetime τ_M, and an analogous average intensity I_M. As shown in **Figure 5a**, τ_M decreases systematically as the mass fraction of PEO increases. A similar decrease in I_M is seen in **Figure 5b**, suggesting that the infiltrating PEO reduces the average pore size and decreases the porosity. MOF-801, with the smallest geometric pores, is the most difficult to fill and appears to retain porosity even at high PEO mass fractions. The intensity data (normalized by mass fraction of PEO) in **Figure 5b** suggests that nearly all surface-accessible pores are filled above 30 % mass fraction PEO loading in UiO-66 samples. If the MOF particles fill from the outside (surface) inwards, then PALS may not be

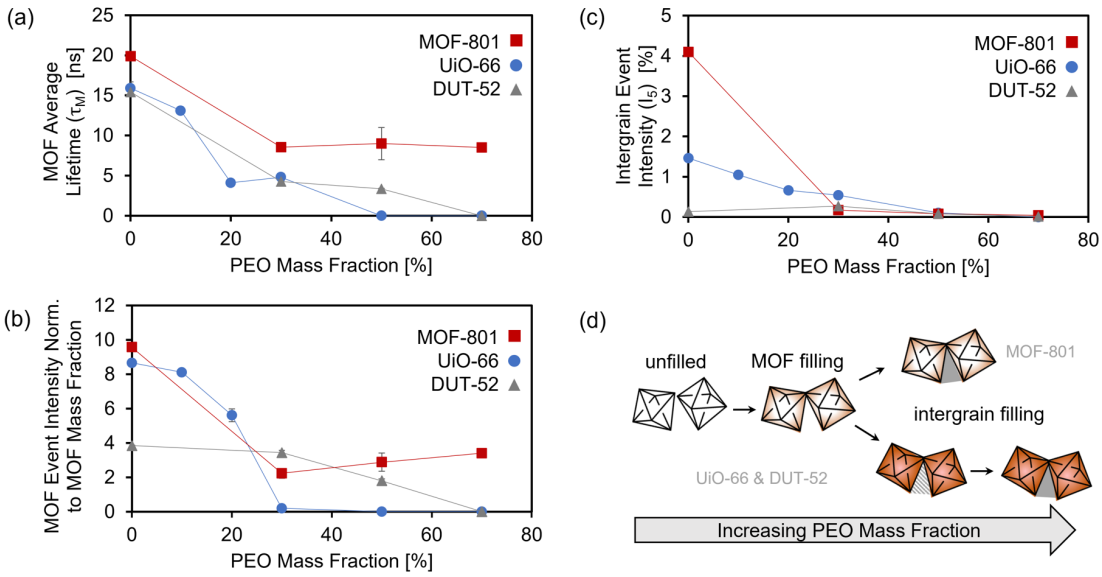

Figure 5. PALS results from MOF/PEO composites. The parameters associated with the MOF pores include the (a) average lifetime before annihilation (τ_M) and (b) the annihilation event intensity (I_M) normalized by the mass fraction of MOF in the sample. As the PEO mass fraction is increased, both the lifetime (a) and intensity (b) of the MOF event are diminished. The intensity of annihilation events corresponding to intergrain locations are presented in (c) with respect to PEO mass fraction. We illustrate our filling hypothesis in the scheme in (d).

sensitive to inaccessible pores deep within the particle.[64] When the PEO mass fraction is decreased below 30 % in UiO-66/PEO composites, these longer lifetimes are apparent (**Figure 5b**), indicating MOF porosity is maintained and pores are at least partially unfilled.

The lifetime and intensity corresponding to positron escape from the material, τ_5 and I_5, describe the empty space between MOF crystallites where long lifetimes (> 100 ns) are expected. I_5 values for both MOF and MOF/PEO samples are plotted in **Figure 5c**. We notice a decrease in I_5 with PEO loading, continuing towards no detection of positron escape in samples containing 70 % mass fraction PEO. Based on the PALS results, we suggest the mechanism of pore filling involves preferential filling of the MOF pores followed by filling of interstitial spaces between crystallites as illustrated in **Figure 5d**. MOF-801 remains partially unfilled even at higher PEO mass fractions and begins to feature characteristics of intergrain filling at lower PEO loadings than UiO-66 and DUT-52. This is consistent with our collective findings from NMR, DSC, and X-ray experiments where the MOF-801/PEO composite had the most PEO outside/not interacting with MOF particles.

Synopsis of Results

The different methods we present provide complementary information from the perspectives of the polymer, MOF, and composite that enable direct structural comparisons both across and within compositional series. We illustrate proposed structural representations based on compiled results in **Scheme 3** for the MOF-801 and UiO-66 versions of the 70/30 MOF/PEO series, which show the greatest structural differences. In composites with low MOF loadings or where infiltration is hindered, excess PEO outside the MOF particles forms crystalline domains in intergrain areas that are found by DSC to be smaller than those formed in the pure PEO film. By analyzing the mass fraction of crystalline PEO outside the MOF, we establish the trend of infiltration in the MOF/PEO series to follow MOF-801 < DUT-52 < UiO-66, where UiO-66 has the most PEO infiltration. Additional temperature modulated DSC experiments reveal a nonmobile amorphous fraction of PEO that follows MOF-801 << DUT-52 < UiO-66, which we ascribe to PEO near MOF in the composite. This fraction of imbibed and MOF-associated PEO is high (0.8 to 0.93) for the 70/30 MOF/PEO composites as quantified from ^{1}H-^{13}C CPMAS NMR measurements and follows the same trend with respect to MOF identity as the DSC results. Additional $T_{1\rho}$ analysis on individual features relates that pore filling is not homogeneous across all particles in the composite and that some degree of underfilling is expected.

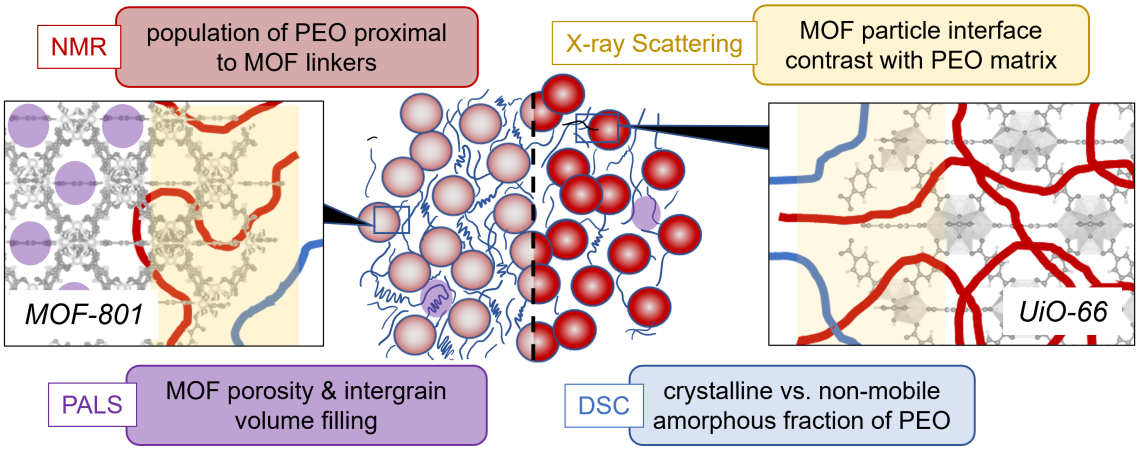

Scheme 3. Representation of the proposed MOF-801 (left) and UiO-66 (right) 70/30 MOF/PEO composite structures. We describe how each technique utilized in this study measures key structural attributes.

From PALS we conclude the MOF pores are infiltrated by PEO first, followed by polymer buildup in the intergrain space between particles. MOF-801, with the tightest pores, retains some MOF-like porosity hinting complete pore filling may be hindered, while both UiO-66 and DUT-52 structures are more fully filled. We identify that the power law decay of X-ray scattering intensities corresponds to changes in electron density at the MOF-matrix interface that are related to the fraction of imbibed PEO within the MOF. Applying this analysis to a series of composites with different MOF/PEO ratios, we demonstrate the relationship is continuous across a compositional series and enables both confirmation and relative comparison of infiltration extent. While power law decay analysis of X-ray may not be as quantitative without further structural modeling as other the methods presented here (NMR, DSC, PALS), we believe it is ideal for use in rapid structure assessment.

Experimental Methods

Certain equipment, instruments, software, or materials are identified in this paper in order to specify the experimental procedure adequately. Such identification is not intended to imply recommendation or endorsement of any product or service by the National Institute of Standards and Technology, nor is it intended to imply that the materials or equipment identified are necessarily the best available for the purpose. The following experimental methods are repeated in the Supporting Information file with additional details.

MOF powders and PEO composites used in this study were prepared by adapting previously reported methods[10], described in the Supporting Information. General MOF and MOF/PEO composite attributes were evaluated via XRD (Bruker D8 Advance diffractometer equipped with an EIGER R2 R 500 K detector from Dectris, Inc.), TGA (TA Instruments Q500 TGA), and solution-state NMR (Bruker AVANCE II 600 MHz spectrometer). Scanning electron micrographs were obtained for the MOF powders using a Bruker Quanta 200 a JEOL 7800F field emission microscope for AuPd-sputtered MOF/PEO composites.

Calorimetric data were collected using a TA Instruments DSC 2500 under a dry nitrogen purge. To analyze the PEO melting event, the temperature was cycled between -60 °C to 80 °C at a ramp rate of 10 °C min^{-1} with 5 min isothermal steps after each ramp step. Data analyses were performed using the TRIOS software. The cycles were repeated a minimum of 4 times, and only the last 3 cycles were included in the analysis. Temperature modulated DSC was performed to enhance resolution of the glass transition. Temperature scans were performed on the samples at heating rates of 3 °C /min with a temperature modulation of 1 °C per 120 s.

X-ray scattering measurements were performed at the X-ray Science Division beamlines at the Advanced Photon Source (APS), Argonne National Laboratory via their user mail-in program. Measurements were carried out using 21 keV X-rays for the incident beam, and scattering data were obtained using three devices for USAXS, SAXS, and WAXS data.[47–49] Flyscan and 2D data were reduced, merged, and analyzed using the software packages developed by APS[50,51].

Solid-state natural abundance ^{13}C NMR spectra of MAS samples were acquired on a Bruker AVANCE NEO 500 MHz NMR spectrometer using the combination of a $T_{1\rho}$ filtered cross-polarization pulse sequence with proton SPINAL-64 decoupling, described previously.[10] ^{13}C NMR spectra were acquired using proton 90° pulse widths of 2.5 μs, contact times of 2 ms and pulse delays of 5 s. Spectra of MAS samples consisting of roughly 50 mg MOF or MOF/PEO composite packed into a 3.2 mm OD rotor were acquired at ambient temperature with spinning frequency of 14 kHz.

The details of the PALS instrument appear elsewhere.[55] PALS measurements were conducted under vacuum environment using a "well" sample holder consisting of ≈ 4 μCi of Na-22 positron source deposited on to a tungsten backing in a 1 mm diameter spot at the bottom of the well. A 2.2 mm thick piece of bulk-metallic glass with a 5 mm diameter hole was mechanically attached to the tungsten bottom to form the well. The sample was loaded into the well and a cover with a pump out hole was placed on top to secure the sample. Spectra were fit using the Positronfit software.

Conclusions

The development of diverse techniques to classify component interactions in MOF-polymer composites (as well as analogous non-MOF systems) is imperative to expand libraries of structural materials knowledge, enabling prediction of compatible MOF-polymer combinations and resulting structure-property relationships. This fundamental study provides a foundation to further develop analytical tools capable of describing the complex chemical and physical attributes of MOF-polymer composites across a multitude of length scales and component characteristics. In addition to guiding characterization efforts in the field, we envision these results will be useful in designing high-throughput classification schemes enabling more efficient design of composites with select attributes for desired applications.

Supporting Information

A supplementary file is available that contains full materials preparation and experimental details, as well as data from XRD, TGA, DSC, NMR, X-ray scattering, and SEM measurements. All references included in the Supplementary Information file have been cited in the main text as well.

Acknowledgements

This research used resources of the Advanced Photon Source, a U.S. Department of Energy (DOE) Office of Science user facility operated for the DOE Office of Science by Argonne National Laboratory, under Contract No. DE-AC02-06CH11357. A.E.B was supported under the National Research Council Research Associateship Program (NRC RAP). We thank the National Science Foundation (NSF-1726058) for funding a solid-state NMR spectrometer at UMD. The authors thank Dr. David Raciti for microscopy assistance.

References

(1) Kalaj, M.; Bentz, K. C.; Ayala, S.; Palomba, J. M.; Barcus, K. S.; Katayama, Y.; Cohen, S. M. MOF-Polymer Hybrid Materials: From Simple Composites to Tailored Architectures. *Chem. Rev.*

2020, *120* (16), 8267–8302. https://doi.org/10.1021/acs.chemrev.9b00575.

(2) Muthukumaraswamy Rangaraj, V.; Wahab, M. A.; Reddy, K. S. K.; Kakosimos, G.; Abdalla, O.; Favvas, E. P.; Reinalda, D.; Geuzebroek, F.; Abdala, A.; Karanikolos, G. N. Metal Organic Framework — Based Mixed Matrix Membranes for Carbon Dioxide Separation: Recent Advances and Future Directions. *Front. Chem.* **2020**, *8*, 1–25. https://doi.org/10.3389/fchem.2020.00534.

(3) Peterson, G. W.; Lee, D. T.; Barton, H. F.; Epps, T. H.; Parsons, G. N. Fibre-Based Composites from the Integration of Metal–Organic Frameworks and Polymers. *Nat. Rev. Mater.* **2021**, *0123456789*. https://doi.org/10.1038/s41578-021-00291-2.

(4) Yang, S.; Karve, V. V.; Justin, A.; Kochetygov, I.; Espín, J.; Asgari, M.; Trukhina, O.; Sun, D. T.; Peng, L.; Queen, W. L. Enhancing MOF Performance through the Introduction of Polymer Guests. *Coord. Chem. Rev.* **2021**, *427*, 213525. https://doi.org/10.1016/j.ccr.2020.213525.

(5) Yao, P.; Yu, H.; Ding, Z.; Liu, Y.; Lu, J.; Lavorgna, M.; Wu, J.; Liu, X. Review on Polymer-Based Composite Electrolytes for Lithium Batteries. *Front. Chem.* **2019**, *7* (August), 1–17. https://doi.org/10.3389/fchem.2019.00522.

(6) Winarta, J.; Meshram, A.; Zhu, F.; Li, R.; Jafar, H.; Parmar, K.; Liu, J.; Mu, B. Metal-Organic Framework-Based Mixed-Matrix Membranes for Gas Separation: An Overview. *J. Polym. Sci.* **2020**, *58* (18), 2518–2546. https://doi.org/10.1002/pol.20200122.

(7) Li, S. C.; Hu, B. C.; Shang, L. M.; Ma, T.; Li, C.; Liang, H. W.; Yu, S. H. General Synthesis and Solution Processing of Metal–Organic Framework Nanofibers. *Adv. Mater.* **2022**, *34* (29). https://doi.org/10.1002/adma.202202504.

(8) Cui, S.; Qin, M.; Marandi, A.; Steggles, V.; Wang, S.; Feng, X.; Nouar, F.; Serre, C. Metal-Organic Frameworks as Advanced Moisture Sorbents for Energy-Efficient High Temperature Cooling. *Sci. Rep.* **2018**, *8* (1), 2–10. https://doi.org/10.1038/s41598-018-33704-4.

(9) Ma, K.; Idrees, K. B.; Son, F. A.; Maldonado, R.; Wasson, M. C.; Zhang, X.; Wang, X.; Shehayeb, E.; Merhi, A.; Kaafarani, B. R.; Islamoglu, T.; Xin, J. H.; Farha, O. K. Fiber Composites of Metal-Organic Frameworks. *Chem. Mater.* **2020**, *32* (17), 7120–7140. https://doi.org/10.1021/acs.chemmater.0c02379.

(10) Duan, P.; Moreton, J. C.; Tavares, S. R.; Semino, R.; Maurin, G.; Cohen, S. M.; Schmidt-Rohr, K. Polymer Infiltration into Metal-Organic Frameworks in Mixed-Matrix Membranes Detected in Situ by NMR. *J. Am. Chem. Soc.* **2019**, *141* (18), 7589–7595. https://doi.org/10.1021/jacs.9b02789.

(11) Rodenas, T.; Van Dalen, M.; García-Pérez, E.; Serra-Crespo, P.; Zornoza, B.; Kapteijn, F.; Gascon, J. Visualizing MOF Mixed Matrix Membranes at the Nanoscale: Towards Structure-Performance Relationships in CO2/CH4 Separation over NH2-MIL-53(Al)@PI. *Adv. Funct. Mater.* **2014**, *24* (2), 249–256. https://doi.org/10.1002/adfm.201203462.

(12) Sabetghadam, A.; Seoane, B.; Keskin, D.; Duim, N.; Rodenas, T.; Shahid, S.; Sorribas, S.; Guillouzer, C. Le; Clet, G.; Tellez, C.; Daturi, M.; Coronas, J.; Kapteijn, F.; Gascon, J. Metal Organic Framework Crystals in Mixed-Matrix Membranes: Impact of the Filler Morphology on the Gas Separation Performance. *Adv. Funct. Mater.* **2016**, *26* (18), 3154–3163. https://doi.org/10.1002/adfm.201505352.

(13) Rodenas, T.; Luz, I.; Prieto, G.; Seoane, B.; Miro, H.; Corma, A.; Kapteijn, F.; Llabrés I Xamena, F. X.; Gascon, J. Metal-Organic Framework Nanosheets in Polymer Composite Materials for Gas Separation. *Nat. Mater.* **2015**, *14* (1), 48–55. https://doi.org/10.1038/nmat4113.

(14) Muldoon, P. F.; Venna, S. R.; Gidley, D. W.; Baker, J. S.; Zhu, L.; Tong, Z.; Xiang, F.; Hopkinson, D. P.; Yi, S.; Sekizkardes, A. K.; Rosi, N. L. Mixed Matrix Membranes from a Microporous Polymer Blend and Nanosized Metal-Organic Frameworks with Exceptional CO2/N2Separation Performance. *ACS Mater. Lett.* **2020**, *2* (7), 821–828. https://doi.org/10.1021/acsmaterialslett.0c00156.

(15) Mizutani, N.; Hosono, N.; Le Ouay, B.; Kitao, T.; Matsuura, R.; Kubo, T.; Uemura, T. Recognition of Polymer Terminus by Metal–Organic Frameworks Enabling Chromatographic Separation of Polymers. *J. Am. Chem. Soc.* **2020**, *142* (8), 3701–3705. https://doi.org/10.1021/jacs.9b13568.

(16) Le Ouay, B.; Watanabe, C.; Mochizuki, S.; Takayanagi, M.; Nagaoka, M.; Kitao, T.; Uemura, T. Selective Sorting of Polymers with Different Terminal Groups Using Metal-Organic Frameworks. *Nat. Commun.* **2018**, *9* (1), 3635. https://doi.org/10.1038/s41467-018-06099-z.

(17) Hosono, N.; Uemura, T. Metal-Organic Frameworks as Versatile Media for Polymer Adsorption and Separation. *Acc. Chem. Res.* **2021**, *54* (18), 3593–3603. https://doi.org/10.1021/acs.accounts.1c00377.

(18) Furukawa, H.; Gándara, F.; Zhang, Y. B.; Jiang, J.; Queen, W. L.; Hudson, M. R.; Yaghi, O. M. Water Adsorption in Porous Metal-Organic Frameworks and Related Materials. *J. Am. Chem. Soc.* **2014**, *136* (11), 4369–4381. https://doi.org/10.1021/ja500330a.

(19) Zhang, W.; Huang, H.; Liu, D.; Yang, Q.; Xiao, Y.; Ma, Q.; Zhong, C. A New Metal-Organic Framework with High Stability Based on Zirconium for Sensing Small Molecules. *Microporous Mesoporous Mater.* **2013**, *171*, 118–124. https://doi.org/10.1016/j.micromeso.2013.01.003.

(20) Øien, S.; Wragg, D.; Reinsch, H.; Svelle, S.; Bordiga, S.; Lamberti, C.; Lillerud, K. P. Detailed Structure Analysis of Atomic Positions and Defects in Zirconium Metal-Organic Frameworks. *Cryst. Growth Des.* **2014**, *14* (11), 5370–5372. https://doi.org/10.1021/cg501386j.

(21) Shearer, G. C.; Chavan, S.; Bordiga, S.; Svelle, S.; Olsbye, U.; Lillerud, K. P. Defect Engineering: Tuning the Porosity and Composition of the Metal-Organic Framework UiO-66 via Modulated Synthesis. *Chem. Mater.* **2016**, *28* (11), 3749–3761. https://doi.org/10.1021/acs.chemmater.6b00602.

(22) Morris, W.; Wang, S.; Cho, D.; Auyeung, E.; Li, P.; Farha, O. K.; Mirkin, C. A. Role of Modulators in Controlling the Colloidal Stability and Polydispersity of the UiO-66 Metal-Organic Framework. *ACS Appl. Mater. Interfaces* **2017**, *9* (39), 33413–33418. https://doi.org/10.1021/acsami.7b01040.

(23) Hu, Z.; Castano, I.; Wang, S.; Wang, Y.; Peng, Y.; Qian, Y.; Chi, C.; Wang, X.; Zhao, D. Modulator Effects on the Water-Based Synthesis of Zr/Hf Metal-Organic Frameworks: Quantitative Relationship Studies between Modulator, Synthetic Condition, and Performance. *Cryst. Growth Des.* **2016**, *16* (4), 2295–2301. https://doi.org/10.1021/acs.cgd.6b00076.

(24) Decker, G. E.; Stillman, Z.; Attia, L.; Fromen, C. A.; Bloch, E. D. Controlling Size, Defectiveness, and Fluorescence in Nanoparticle UiO-66 through Water and Ligand Modulation. *Chem. Mater.* **2019**, *31* (13), 4831–4839. https://doi.org/10.1021/acs.chemmater.9b01383.

(25) DeStefano, M. R.; Islamoglu, T.; Garibay, S. J.; Hupp, J. T.; Farha, O. K. Room-Temperature Synthesis of UiO-66 and Thermal Modulation of Densities of Defect Sites. *Chem. Mater.* **2017**, *29* (3), 1357–1361. https://doi.org/10.1021/acs.chemmater.6b05115.

(26) Valenzano, L.; Civalleri, B.; Chavan, S.; Bordiga, S.; Nilsen, M. H.; Jakobsen, S.; Lillerud, K. P.;

Lamberti, C. Disclosing the Complex Structure of UiO-66 Metal Organic Framework: A Synergic Combination of Experiment and Theory. *Chem. Mater.* **2011**, *23* (7), 1700–1718. https://doi.org/10.1021/cm1022882.

(27) Shearer, G. C.; Forselv, S.; Chavan, S.; Bordiga, S.; Mathisen, K.; Bjørgen, M.; Svelle, S.; Lillerud, K. P. In Situ Infrared Spectroscopic and Gravimetric Characterisation of the Solvent Removal and Dehydroxylation of the Metal Organic Frameworks UiO-66 and UiO-67. *Top. Catal.* **2013**, *56* (9–10), 770–782. https://doi.org/10.1007/s11244-013-0027-0.

(28) Semino, R.; Moreton, J. C.; Ramsahye, N. A.; Cohen, S. M.; Maurin, G. Understanding the Origins of Metal-Organic Framework/Polymer Compatibility. *Chem. Sci.* **2018**, *9* (2), 315–324. https://doi.org/10.1039/c7sc04152g.

(29) Kang, M.; Kim, T. H.; Han, H. H.; Min, H. J.; Bae, Y. S.; Kim, J. H. Submicron-Thick, Mixed-Matrix Membranes with Metal-Organic Frameworks for CO2 Separation: MIL-140C vs. UiO-67. *J. Memb. Sci.* **2022**, *659* (July), 120788. https://doi.org/10.1016/j.memsci.2022.120788.

(30) Kathuria, A.; Brouwers, N.; Buntinx, M.; Harding, T.; Auras, R. Effect of MIL-53 (Al) MOF Particles on the Chain Mobility and Crystallization of Poly(L-Lactic Acid). *J. Appl. Polym. Sci.* **2018**, *135* (3), 1–8. https://doi.org/10.1002/app.45690.

(31) Buckley, C. P.; Kovacs, A. J. Melting Behaviour of Low Molecular Weight Poly (Ethylene-Oxide) Fractions. In *Progress in Colloid & Polymer Science*; Steinkopff: Darmstadt, 1975; Vol. 58, pp 44–52. https://doi.org/10.1007/BFb0117122.

(32) Wunderlich, B. Reversible Crystallization and the Rigid–Amorphous Phase in Semicrystalline Macromolecules. *Prog. Polym. Sci.* **2003**, *28* (3), 383–450. https://doi.org/10.1016/S0079-6700(02)00085-0.

(33) Crist, B.; Mirabella, F. M. Crystal Thickness Distributions from Melting Homopolymers or Random Copolymers. *J. Polym. Sci. Part B Polym. Phys.* **1999**, *37* (21), 3131–3140. https://doi.org/10.1002/(SICI)1099-0488(19991101)37:21<3131::AID-POLB22>3.0.CO;2-M.

(34) Wunderlich, B. *Macromolecular Physics: Crystal Melting*; Academic Press: New York, 1980.

(35) Bartolotta, A.; Di Marco, G.; Lanza, M.; Carini, G. The Fusion of Ethylene Oxide Polymers. *Nuovo Cim. D* **1994**, *16* (7), 825–830. https://doi.org/10.1007/BF02456730.

(36) Huggins, M. L. Certain Properties of Long-Chain Compounds as Functions of Chain Length. *J. Phys. Chem.* **1939**, *43* (8), 1083–1098. https://doi.org/10.1021/j150395a010.

(37) Broadhurst, M. G. An Analysis of the Solid Phase Behavior of the Normal Paraffins. *J. Res. Natl. Bur. Stand. Sect. A Phys. Chem.* **1962**, *66* (3), 241–249. https://doi.org/10.6028/jres.066a.024.

(38) Takahashi, Y.; Tadokoro, H. Structural Studies of Polyethers, (-(CH 2)m-O-) n . X. Crystal Structure of Poly(Ethylene Oxide). *Macromolecules* **1973**, *6* (5), 672–675. https://doi.org/10.1021/ma60035a005.

(39) Kienzle, P. A.; Krycka, J.; Patel, N.; Sahin, I. Bumps. University of Maryland: College Park, MD 2011.

(40) Fritzsching, K. J.; Mao, K.; Schmidt-Rohr, K. Avoidance of Density Anomalies as a Structural Principle for Semicrystalline Polymers: The Importance of Chain Ends and Chain Tilt. *Macromolecules* **2017**, *50* (4), 1521–1540. https://doi.org/10.1021/acs.macromol.6b02000.

(41) Hartmann, S. R.; Hahn, E. L. Nuclear Double Resonance in the Rotating Frame. *Phys. Rev.* **1962**,

128 (5), 2042–2053. https://doi.org/10.1103/PhysRev.128.2042.

(42) Johansson, A.; Tegenfeldt, J. NMR Study of Crystalline and Amorphous Polyethylene Oxide). *Macromolecules* **1992**, *25* (18), 4712–4715. https://doi.org/10.1021/ma00044a036.

(43) Clauss, J.; Schmidt-Rohr, K.; Spiess, H. W. Determination of Domain Sizes in Heterogeneous Polymers by Solid-state NMR. *Acta Polym.* **1993**, *44* (1), 1–17. https://doi.org/10.1002/actp.1993.010440101.

(44) Nieuwendaal, R. C.; Wilbur, J. D.; Welsh, D.; Witherspoon, V.; Stafford, C. M. A Method to Quantify Composition, Purity, and Cross-Link Density of the Active Polyamide Layer in Reverse Osmosis Composite Membranes Using 13C Cross Polarization Magic Angle Spinning Nuclear Magnetic Resonance Spectroscopy. *J. Memb. Sci.* **2022**, 120346. https://doi.org/10.1016/j.memsci.2022.120346.

(45) Johnson, R. L.; Schmidt-Rohr, K. Quantitative Solid-State 13C NMR with Signal Enhancement by Multiple Cross Polarization. *J. Magn. Reson.* **2014**, *239*, 44–49. https://doi.org/10.1016/j.jmr.2013.11.009.

(46) Chu, B.; Hsiao, B. S. Small-Angle X-Ray Scattering of Polymers. *Chem. Rev.* **2001**, *101* (6), 1727–1761. https://doi.org/10.1021/cr9900376.

(47) Ilavsky, J.; Zhang, F.; Andrews, R. N.; Kuzmenko, I.; Jemian, P. R.; Levine, L. E.; Allen, A. J. Development of Combined Microstructure and Structure Characterization Facility for in Situ and Operando Studies at the Advanced Photon Source Research Papers. *J. Appl. Crystallogr.* **2018**, *51*, 867–882. https://doi.org/10.1107/S160057671800643X.

(48) Ilavsky, J.; Jemian, P. R.; Allen, A. J.; Zhang, F.; Levine, L. E.; Long, G. G. Ultra-Small-Angle X-Ray Scattering at the Advanced Photon Source. *J. Appl. Crystallogr.* **2009**, *42* (3), 469–479. https://doi.org/10.1107/S0021889809008802.

(49) Ilavsky, J.; Zhang, F.; Allen, A. J.; Levine, L. E.; Jemian, P. R.; Long, G. G. Ultra-Small-Angle X-Ray Scattering Instrument at the Advanced Photon Source: History, Recent Development, and Current Status. *Metall. Mater. Trans. A Phys. Metall. Mater. Sci.* **2013**, *44* (1), 68–76. https://doi.org/10.1007/s11661-012-1431-y.

(50) Ilavsky, J. Nika: Software for Two-Dimensional Data Reduction. *J. Appl. Crystallogr.* **2012**, *45* (2), 324–328. https://doi.org/10.1107/S0021889812004037.

(51) Ilavsky, J.; Jemian, P. R. Irena: Tool Suite for Modeling and Analysis of Small-Angle Scattering. *J. Appl. Crystallogr.* **2009**, *42* (2), 347–353. https://doi.org/10.1107/S0021889809002222.

(52) Kline, S. R. Reduction and Analysis of SANS and USANS Data Using IGOR Pro. *J. Appl. Crystallogr.* **2006**, *39* (6), 895–900. https://doi.org/10.1107/S0021889806035059.

(53) Boldon, L.; Laliberte, F.; Liu, L. Review of the Fundamental Theories behind Small Angle X-Ray Scattering, Molecular Dynamics Simulations, and Relevant Integrated Application. *Nano Rev.* **2015**, *6* (1), 25661. https://doi.org/10.3402/nano.v6.25661.

(54) Porod, V. G. Die Rontgenkleinwinkelstreuung von Dichtgepackten Kolloiden Systemen Einleitung. *Kolloid-Zeitschrift* **1951**, *124*, 83–114. https://doi.org/10.1007/BF01512792.

(55) Gidley, D. W.; Peng, H.; Vallery, R. S. Positron Annihilation as a Method to Characterize Porous Materials. *Annu. Rev. Mater. Res.* **2006**, *36* (1), 49–79. https://doi.org/10.1146/annurev.matsci.36.111904.135144.

(56) Liu, M.; Wong-Foy, A. G.; Valleiy, R. S.; Frieze, W. E.; Schnobrich, J. K.; Gidley, D. W.; Matzger, A. J. Evolution of Nanoscale Pore Structure in Coordination Polymers during Thermal and Chemical Exposure Revealed by Positron Annihilation. *Adv. Mater.* **2010**, *22* (14), 1598–1601. https://doi.org/10.1002/adma.200903618.

(57) Eldrup, M.; Lightbody, D.; Sherwood, J. N. The Temperature Dependence of Positron Lifetimes in Solid Pivalic Acid. *Chem. Phys.* **1981**, *63*, 51–58. https://doi.org/10.1016/0301-0104(81)80307-2.

(58) Tao, S. J. Positronium Annihilation in Molecular Substances. *J. Chem. Phys.* **1972**, *56*, 5499–5510. https://doi.org/10.1063/1.1677067.

(59) Machado, J. C.; Silva, G. G.; Oliveira, F. C. de; Lavall, R. L.; Rieumont, J.; Licinio, P.; Windmöller, D. Free-Volume and Crystallinity in Low Molecular Weight Poly(Ethylene Oxide). *J. Polym. Sci. Part B Polym. Phys.* **2007**, *45* (17), 2400–2409. https://doi.org/10.1002/polb.21242.

(60) Stassin, T.; Verbeke, R.; Cruz, A. J.; Rodríguez-Hermida, S.; Stassen, I.; Marreiros, J.; Krishtab, M.; Dickmann, M.; Egger, W.; Vankelecom, I. F. J.; Furukawa, S.; De Vos, D.; Grosso, D.; Thommes, M.; Ameloot, R. Porosimetry for Thin Films of Metal–Organic Frameworks: A Comparison of Positron Annihilation Lifetime Spectroscopy and Adsorption-Based Methods. *Adv. Mater.* **2021**, *33* (17), 2006993. https://doi.org/10.1002/adma.202006993.

(61) Mor, J.; Utpalla, P.; Bahadur, J.; Sen, D.; Sharma, S. K. Porosimetry of Zeolitic Imidazolate Frameworks Using Positron Annihilation Lifetime Spectroscopy. *Microporous Mesoporous Mater.* **2023**, *348* (December 2022), 112389. https://doi.org/10.1016/j.micromeso.2022.112389.

(62) Yuan, L.; Tian, M.; Lan, J.; Cao, X.; Wang, X.; Chai, Z.; Gibson, J. K.; Shi, W. Defect Engineering in Metal–Organic Frameworks: A New Strategy to Develop Applicable Actinide Sorbents. *Chem. Commun.* **2018**, *54* (4), 370–373. https://doi.org/10.1039/C7CC07527H.

(63) Mahdavi, H.; Eden, N. T.; Doherty, C. M.; Acharya, D.; Smith, S. J. D.; Mulet, X.; Hill, M. R. Underlying Polar and Nonpolar Modification MOF-Based Factors That Influence Permanent Porosity in Porous Liquids. *ACS Appl. Mater. Interfaces* **2022**, *14* (20), 23392–23399. https://doi.org/10.1021/acsami.2c03082.

(64) Feldblyum, J. I.; Liu, M.; Gidley, D. W.; Matzger, A. J. Reconciling the Discrepancies between Crystallographic Porosity and Guest Access As Exemplified by Zn-HKUST-1. *J. Am. Chem. Soc.* **2011**, *133*, 18257–18263. https://doi.org/10.1021/ja2055935.

TOC Graphic

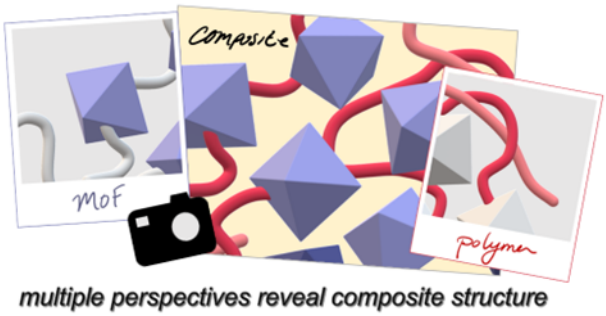

multiple perspectives reveal composite structure